THE JOURNAL OF BIOLOGICAL CHEMISTRY VOL. 289, NO. 24, pp. 17240–17248, June 13, 2014

Crystallin-αB Regulates Skeletal Muscle Homeostasis via Modulation of Argonaute2 Activity*

Received for publication, January 10, 2014, and in revised form, April 28, 2014 Published, JBC Papers in Press, April 29, 2014, DOI 10.1074/jbc.M114.549584

Ronald L. Neppl[‡§1,2], **Masaharu Kataoka**[‡§1], **and Da-Zhi Wang**[‡§¶3]

From the [‡]*Department of Cardiology, Boston Children's Hospital and* [§]*Department of Pediatrics, Harvard Medical School, Boston, Massachusetts 02115 and the* [¶]*Harvard Stem Cell Institute, Harvard University, Cambridge, Massachusetts 02138*

Background: Regulation of gene expression at the post-transcriptional level by RNAi is necessary for development and cellular homeostasis.
Results: Aged Crystallin-αB null mice develop skeletal muscle atrophy, whereas young mice are biased toward atrophy.
Conclusion: Crystallin-αB is a novel and necessary component of skeletal muscle RISC.
Significance: A molecular mechanism by which deleterious regulation of Argonaute2 activity contributes to defects in skeletal muscle homeostasis and regeneration.

The core functional machinery of the RNAi pathway is the RNA-induced silencing complex (RISC), wherein Argonaute2 (Ago2) is essential for siRNA-directed endonuclease activity and RNAi/microRNA-mediated gene silencing. Crystallin-αB (CryAB) is a small heat shock protein involved in preventing protein aggregation. We demonstrate that CryAB interacts with the N and C termini of Ago2, not the catalytic site defined by the convergence of the PAZ, MID, and PIWI domains. We further demonstrate significantly reduced Ago2 activity in the absence of CryAB, highlighting a novel role of CryAB in the mammalian RNAi/microRNA pathway. In skeletal muscle of CryAB null mice, we observe a shift in the hypertrophy-atrophy signaling axis toward atrophy under basal conditions. Moreover, loss of CryAB altered the capability of satellite cells to regenerate skeletal muscle. These studies establish that CryAB is necessary for normal Ago2/RISC activity and cellular homeostasis in skeletal muscle.

MicroRNAs (miRNAs)[4] are short (~22-nucleotide) RNA molecules that collectively regulate the expression of ~30% of human genes by directing the RNA-induced silencing complex (RISC) to the 3′-untranslated region (UTR) of protein coding genes (1, 2). RISC is a multiprotein complex capable of repressing the translation of mRNA into protein via a variety of mechanisms including removal of the 5′-7-methylguanylate cap (m^7G), deadenylation of the 3′-poly(A) tail, and miRNA site-directed endonuclease cleavage of the mRNA (3, 4). Argonaute proteins, of which Argonaute2 (Ago2) exclusively has endonuclease activity, form the central core of RISC by bringing the miRNA into close proximity of the target mRNA such that complementary binding of the miRNA, either in its entirety or in its "seed region," may activate RISC activity toward the target mRNA (5–8). MiRNAs act to "fine tune" protein expression to maintain cellular homeostasis and adapt to cellular stresses (9, 10). In the *Drosophila melanogaster* model system, multiple RISC-associated proteins have been identified that either potentiate or inhibit miRNA-directed RISC activity (11–13). However, little is known of mammalian RISC accessory proteins that facilitate normal miRNA-directed RISC activity or how mutations of these proteins may alter normal activity.

The small heat shock protein (sHSP) Crystallin-αB/*Hspb5* (CryAB) contains the highly conserved crystallin domain at its C terminus and is known to assemble into multimeric complexes with a variable number (12-mer to 32-mer) of subunits (14–16). CryAB functions as a molecular chaperone preventing aggregation of partially folded polypeptides and is implicated in multiple neuropathological diseases including multiple sclerosis and Alzheimer disease (17–19). An arginine-to-glycine missense mutation at amino acid position 120 (R120G) has been found to co-segregate with Desmin-related myopathy, an inherited neuromuscular disorder characterized by adult onset of muscle weakening and the accumulation of Desmin protein aggregates in cardiac and skeletal muscles (20, 21). Mice expressing cardiac restricted CryAB R120G develop Desmin-related myopathy due to increased glucose-6-phosphate dehydrogenase (G6PD) activity and "reductive stress" (22, 23). Although much has been learned regarding the perturbations to normal physiology resulting from CryAB mutations, the molecular mechanism by which CryAB participates in these biological activities is not fully understood. As such, we focused on elucidating the molecular mechanisms of skeletal muscle homeostasis and regeneration in which CryAB plays a central role.

* This work was supported by the National Institutes of Health Grant HL110666 (to R. L. N.), as well as National Institutes of Health Grants HL085635 and HL116919 (to D. Z. W.) and the March of Dimes Foundation (to D. Z. W.). This work was also supported by Banyu Life Science Foundation International (to M. K.).
[1] Both authors contributed equally to this work.
[2] To whom correspondence may be addressed: Dept. of Cardiology, Boston Children's Hospital, Harvard Medical School, John F. Enders Research Bldg., 320 Longwood Ave., Boston MA 02115. E-mail: rneppl@enders.tch.harvard.edu.
[3] An Established Investigator of the American Heart Association. To whom correspondence may be addressed: Dept. of Cardiology, Boston Children's Hospital, Harvard Medical School, John F. Enders Research Bldg., 320 Longwood Ave., Boston MA 02115. E-mail: dwang@enders.tch.harvard.edu.
[4] The abbreviations used are: miRNA, microRNA; miR, microRNA; RISC, RNA-induced silencing complex; CryAB, Crystallin-αB; EdU, 5-ethynyl-2′-deoxyuridine; dKO, double knock-out; HET, heterozygous; SC, satellite cell; CTX, cardiotoxin; TA, tibialis anterior.

EXPERIMENTAL PROCEDURES

CryAB Animal Model—Mice in which both the *Cryab* and the neighboring *Hspb2* genes are mutated have been described previously (24).

Fluorescence-activated Cell Sorter (FACS) Analysis—FACS was performed according to methods previously described (25). Cells were detected and analyzed with BD FACSAria.

Immunochemistry—Hind limb muscles were excised, fixed in 4% paraformaldehyde, cut transversely, embedded in paraffin, sectioned, and subjected to immunostaining. Antibody sources were as follows: Pax7 (Developmental Studies Hybridoma Bank (DSHB), 1:150) and laminin (Sigma, 1:1000). Alexa Fluor 488, 546, and 647 (Life Technologies, 1:500) were used as secondary antibodies. Fluorescently stained slides were counterstained with DAPI and imaged with Nikon TE2000/Volocity. Images were minimally manipulated in Photoshop to linearly increase contrast equally across all pixels.

Histological Analysis—Average myofiber cross-sectional area and quantification of fibrosis were calculated as described previously (26, 27). Briefly, hind limb muscle sections were stained with Picro-Sirius Red, collagen volume fraction was determined, and then muscle area was calculated and divided by the number of muscle fibers present in the field to obtain the average fiber size for a given field.

Cell Culture, Plasmids, and Co-immunoprecipitation Assays—HEK293T cells were transfected with Myc- and/or FLAG-tagged Argonaute1 (Ago1, NM_012199.2), Argonatue2 (Ago2, NM_012154.3), Dicer (Addgene 19873), DGCR8 (NM_001190326.1), and Cryab (NM_001885.1) using Lipofectamine 2000 (Life Technologies) or X-tremeGENE 9 (Roche Applied Science). Cells were lysed in 40 mM Tris, pH 7.4, 150 mM NaCl, and 1% Triton X-100 and cleared by centrifugation at 10,000 × *g* for 10 min at 4 °C. Cleared lysates were diluted 1:3 with lysis buffer and incubated with either EZview Red anti-c-Myc or anti-FLAG affinity gel (Sigma Aldrich) at 4 °C for 6 h with gentle rocking. Beads were subsequently washed five times with 40 mM Tris, pH 7.4, 1 M NaCl, 1% Triton X-100, 1 mM DTT or five times with 40 mM Tris, pH 7.4, 1.75 M NaCl, 1% Triton X-100, 1 mM DTT for protein-protein interactions and Ago2-domain interactions, respectively. C0mplete EDTA-free protease inhibitor (Roche Applied Science) was present in all solutions from initial lysis to final wash. Beads were resuspended in 50 μl of 2× Laemmli buffer and stored at −20 °C until analysis by SDS-PAGE and Western blot analysis.

Western Blot Analysis—Tissues were homogenized in 40 mM Tris, pH 7.4, 150 mM NaCl, 1% Triton X-100, and C0mplete EDTA-free protease inhibitor (Roche Applied Science) and cleared by centrifugation at 10,000 × *g* for 10 min at 4 °C. Protein content was determined by the DC protein assay (Bio-Rad) with known concentrations of BSA as standards. Protein concentrations were equalized by the addition of an appropriate volume of lysis buffer. Primary antibody was visualized with either IRDye 680RD goat anti-mouse or IRDye 800CW goat anti-rabbit (LI-COR) on the Odyssey imaging system (LI-COR Biosciences).

In Vivo Cell Proliferation—5-Ethynyl-2′-deoxyuridine (EdU, 5 μg/g of body weight) was injected into mice intraperitoneally 24 and 16 h prior to muscle isolation. Following fixation and embedding, EdU was detected using the Click-iT® EdU Alexa Fluor® 488 imaging kit (Life Technologies).

Tissue Lysates for RNA Cleavage Assays—Skeletal muscle lysates were prepared from 8–10-week WT and CryAB dKO mice as described (5) with the following modifications for tissues. 500–700 mg of hind limb skeletal muscle was cleaned of adventitia and homogenized in ~8 ml of buffer containing 10 mM HEPES-NaOH, pH 7.9,10 mM KCl, 1.5 mM $MgCl_2$, 0.5 mM 4-(2-aminoethyl) benzenesulfonyl fluoride hydrochloride (AEBSF), and 0.1 mM DTT. Following homogenization, lysates were incubated on ice for 10 min and centrifuged at 5,000 × *g* for 10 min at 4 °C. The supernatants were transferred to clean tubes and further cleared by ultracentrifugation at 30,000 × *g* for 30 min at 4 °C to obtain the cleared cytoplasmic lysate. Protein concentration was determined using the DC protein assay (Bio-Rad). Known concentrations of BSA were used as standards. Cleared lysates from WT and dKO mice were equalized by the addition of lysis buffer. The lysate concentration of KCl was raised to 100 mM by the addition of 2.5 M KCl. Glycerol was then added to a final concentration of 10%. Lysates were aliquoted, flash-frozen in liquid nitrogen, and stored at −80 °C until use.

In Vitro Transcription and Addition of 5′-m^7G Cap—Fragments of previously described miRNA sensor constructs (28) were amplified by PCR and ligated into pcDNA 3.1 vector. Circular plasmids were linearized for T7 run-off transcription. Following purification, RNA content was quantified and 5′-capped using the Vaccinia capping system (New England Biolabs). The reaction was stopped by the addition of 1 ml of TRIzol reagent. 5′-capped RNA was quantified and stored at −80 °C until use.

In Vitro miRNA-directed RNA Cleavage—miRNA-directed RNA cleavage was performed as described previously (5) with the following modifications. RNA target was added to 50-μl reactions containing 50% cleared skeletal muscle lysate, 1 mM ATP, 0.2 mM GTP, 10 units/ml RNasin (Promega) in 100 mM KCl, 1.5 mM $MgCl_2$, 0.1 mM DTT, 10 mM HEPES-NaOH (pH 7.9), and 5 nM miRNA at 30 °C. 0.5 pmol (10 nM final concentration) of capped RNA target was added after miRNA was allowed to preincubate with cleared lysate reaction mixture for 20 min at 30 °C. Reactions were stopped by the addition of 1 ml of TRIzol reagent (Life Technologies).

Northern Blot Analysis and Quantification—Purified RNA from *in vitro* miRNA-directed cleavage assays and total RNA from both WT and dKO hind limb skeletal muscle were separated according to size in denaturing 6 and 15% polyacrylamide gels, respectively, and transferred to Zeta-Probe membrane as described previously (29). Purified RNA from the miRNA-214 target cleavage assay was separated according to size on a 1.25% denaturing agarose gel and transferred to Zeta-Probe membrane. ^{32}P-labeled probes were hybridized overnight and washed with successive increasingly stringent SSC/0.1% SDS buffers. ^{32}P-signal was detected and quantified using a PhosphorImager.

Arogonaute2 RNA Immunoprecipitation—Hind limb skeletal muscles from WT and dKO littermates (8–10 weeks of age) were homogenized in 50 mM Tris, pH 7.5, 5 mM EDTA, 5 mM EGTA, 1 mg/ml yeast tRNA, and 50 units/ml RNase inhibitor (Promega). Following homogenization, lysates were centrifuged at 1000 × *g* for 10 min at 4 °C. Supernatants were transferred to clean tubes, Nonidet P-40 was added to a final con-

centration of 0.5% and incubated for 15 min at 4 °C with gentle rocking, and the lysates were centrifuged at 10,000 × *g* for 10 min at 4 °C. The supernatants were transferred to clean tubes, protein concentrations were measured using the DC protein assay (Bio-Rad), and the protein concentrations of the lysates were then equalized by the addition of lysis buffer. Mouse monoclonal anti-Ago2 (5 μg, Wako Chemical) and 5 μg of mouse IgG were added to equal volumes of the final WT and dKO lysates and incubated overnight at 4 °C. Antibody-bound proteins were precipitated by the addition of protein G Dynabeads (Life Technologies) at 4 °C. Beads were washed four times with lysis buffer supplemented with 0.5% Nonidet P-40. One-fifth of the beads were resuspended in 50 μl of 2× Laemmli buffer and stored at −20 °C until analysis by SDS-PAGE and Western blot analysis. The remainder of the beads was resuspended in 1 ml of TRIzol reagent (Life Technologies). MicroRNA TaqMan quantitative PCR was performed according to previously established methods (28) and normalized to total immunoprecipitated Ago2 protein.

Luciferase Reporter Assay—HEK293T cells were transiently transfected with miR-1 and Luc-HDAC4 3′-UTR reporter (30) as well as miR-208 and Luc-miR208 sensor (31), in the presence and absence of Cryab expression vector. Luciferase reporter assay was performed according to manufacturer's instructions (Promega).

RESULTS

CryAB Is Necessary for the Maintenance of Myofiber Size—CryAB null mice, in which both *Cryab* and the neighboring *Hspb2* gene were mutated and herein named CryAB dKO, at ~1 year of age exhibit significantly reduced body weight and muscle atrophy (Fig. 1, *A* and *B*), consistent with a prior study (24). In addition, histological examination of hind limb skeletal muscle indicates periodic necrotic regions (Fig. 1*C*) with significantly reduced myofiber cross-sectional area (Fig. 1, *C* and *E*) and significantly increased fibrosis (Fig. 1, *D* and *F*). Consistent with these observations, Western blot analysis indicates dramatically reduced expression of myosin heavy chain in skeletal muscle of CryAB dKO mice (Fig. 1*G*). We utilized FACS analysis to quantify satellite cells (SCs) isolated from the mononuclear fraction of ~1-year mouse hind limb skeletal muscle. Interestingly, we observe a dramatic decrease in the SC percentage in CryAB dKO mouse as compared with both WT and HET (Fig. 1*H*).

CryAB dKO Mice Exhibit Satellite Cell Hyperplasia and Myofiber Hypotrophy following Acute Muscle Injury—We asked whether skeletal muscles of young CryAB dKO mice display similar morphological deficits as observed in aged mice. In contrast to ~1-year-old mice, we observe no myofibril defects in H&E-stained sections of 8-week-old WT, HET, and dKO skeletal muscle (Fig. 2*A*, *top*). In addition, little or no fibrosis is observed in CryAB dKO muscle as indicated by Sirius Red (Fig. 2*A*, *bottom*). SC quantification by FACS analysis indicates no significant difference in the percentage of SCs in the mononuclear fraction between 8-week-old WT (45.03 ± 6.22%), HET (48.33 ± 9.13%), and dKO (53.17 ± 2.66%) littermates (Fig. 2*B*). Our observed SC percentages are in agreement with previously quantified SC content in adult mice (32).

Next, we used the cardiotoxin (CTX) injury model to test whether loss of CryAB affects satellite cell-dependent skeletal muscle regeneration. We injected CTX into the right tibialis anterior (TA) muscle with an equal volume of sterile saline injected into the left TA muscle as control. We observe a significant decrease in the average myofiber cross-sectional area in CryAB dKO mice 14 days following CTX injection as compared with WT and HET littermates (Fig. 2, *C* and *E*). Additionally, we observe a significant increase in fibrosis in CryAB dKO mice following CTX injection (Fig. 2, *C* and *F*). Saline-injected controls showed no significant differences in either average myofiber cross-sectional area or extracellular fibrosis (data not shown). Unexpectedly, we observe a nearly 3-fold increase in the SC percentage of the mononuclear fraction (CTX-injected TA muscle as compared with the sterile saline-injected TA muscle) in dKO mice as compared with WT littermates (Fig. 2*D*). We also observe a similar significant increase of ~1.6-fold in HET mice as compared with WT littermates. Together, these results indicate that CryAB is necessary for normal skeletal muscle regeneration.

To further explore our observed SC hyperplasia, we again challenged mice with CTX and injected EdU 24 and 16 h prior to the 14-day time point to determine whether the SCs were actively proliferating or remnants of an initial proliferative burst following CTX injury. We observe EdU incorporation in nuclei inside the laminin signal indicative of the SC niche (Fig. 3*A*). EdU-positive signal is significantly ($p < 0.05$) increased from 0.037 ± 0.053 EdU-positive nuclei per fiber in WT mice to 0.249 ± 0.137 EdU-positive nuclei per fiber in CryAB dKO. We next sought to determine whether our observed increase in SCs was due to increased proliferative or decreased anti-proliferative signaling. To accomplish this, we isolated RNA from the left TA (saline) and right TA (CTX) muscles of WT and dKO littermates to examine the expression of cell proliferation regulatory genes. At the 14-day time point, we observe no significant difference in the expression of p21 in dKO mice as compared with WT, but observe a significant slight ~10% decrease in the expression of p27 (Fig. 3*B*). Following CTX injection, p21 is found to increase to ~250% of the saline-injected control in WT mice, whereas it is significantly decreased to ~85% of control in dKO mice (Fig. 3*B*). Notch signaling was previously demonstrated to inhibit SC proliferation and promote differentiation of myogenic cells (33, 34), and we similarly observe significant perturbations in Notch signaling under basal and regenerative conditions in dKO mice (Fig. 3*C*). Together, these data suggest that under basal conditions, and during regeneration, genetic ablation of CryAB leads to a pro-proliferative gene expression repertoire.

CryAB dKO Mice Are Biased toward Proliferative and Atrophic Signaling—We examined the expression of molecular markers for satellite cell and activated myoblasts. Although there is no statistical difference in the basal expression of *Pax7* in dKO mice as compared with WT littermates (Fig. 3*D*), we do observe less Pax7 protein expression under basal conditions in dKO mice (Fig. 3*F*). Interestingly, we observe ~270% increase in *Myf5* gene expression in WT mice 14 days following CTX injection (Fig. 3*D*) without a corresponding increase in Myf5 protein content (Fig. 3*F*). Further, Myf5 protein content is

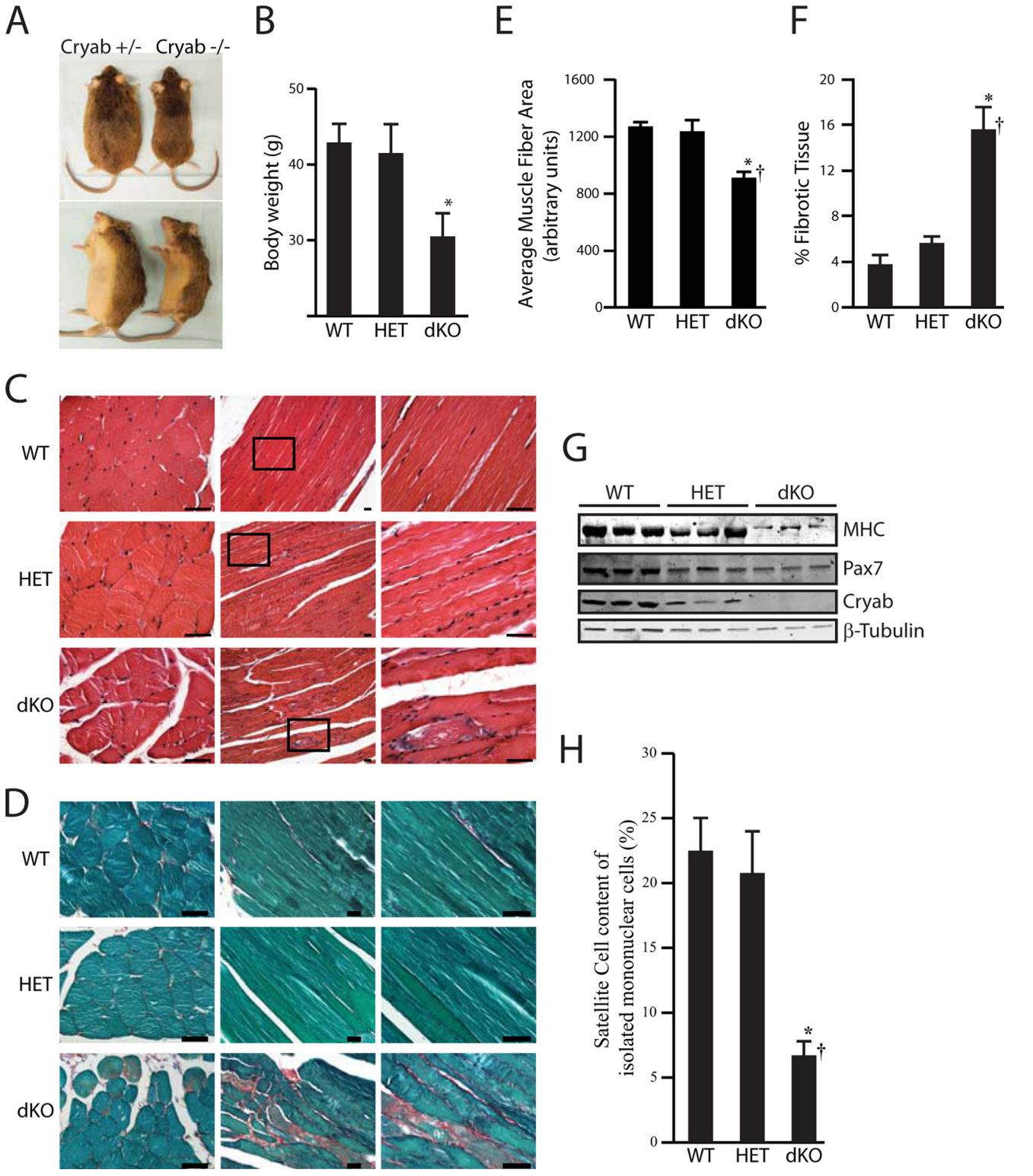

FIGURE 1. **Skeletal muscle from Cryab dKO mice exhibit age-dependent atrophy and reduced regeneration potential.** *A* and *B*, body size of litter mates at ~1 year of age (*A*) and body weight analysis by genotype (*B*). *C* and *D*, histological analysis by H&E (*C*) and Sirius Red (*D*) staining of skeletal muscle from Cryab WT, HET, and dKO mice. *F*, quantification of average muscle fiber cross-sectional area (*E*) and percentage of fibrotic tissue area (*F*). *G*, Western analysis of hind limb skeletal muscle lysates. *H*, FACS analysis of satellite cell content expressed as a percentage of the mononuclear fraction. Analyses were performed with littermates at ~1 year of age (*A–H*) unless otherwise indicated. *Scale bars* are 50 μm. Statistical significance was set at $p < 0.05$ (*, with respect to WT, $n = 3$), and $p < 0.05$ (†, with respect to HET, $n = 3$). *MHC*, myosin heavy chain.

reduced in dKO mice as compared with WT littermates under basal conditions (Fig. 3*F*), although *Myf5* mRNA was quantified to be increased by ~12% (Fig. 3*D*). In addition, the myogenic factors *Mef2a* and *Mef2c* are similarly dysregulated under basal and regenerative conditions (Fig. 3*D*). Together, these results would suggest that the altered expression of these key satellite

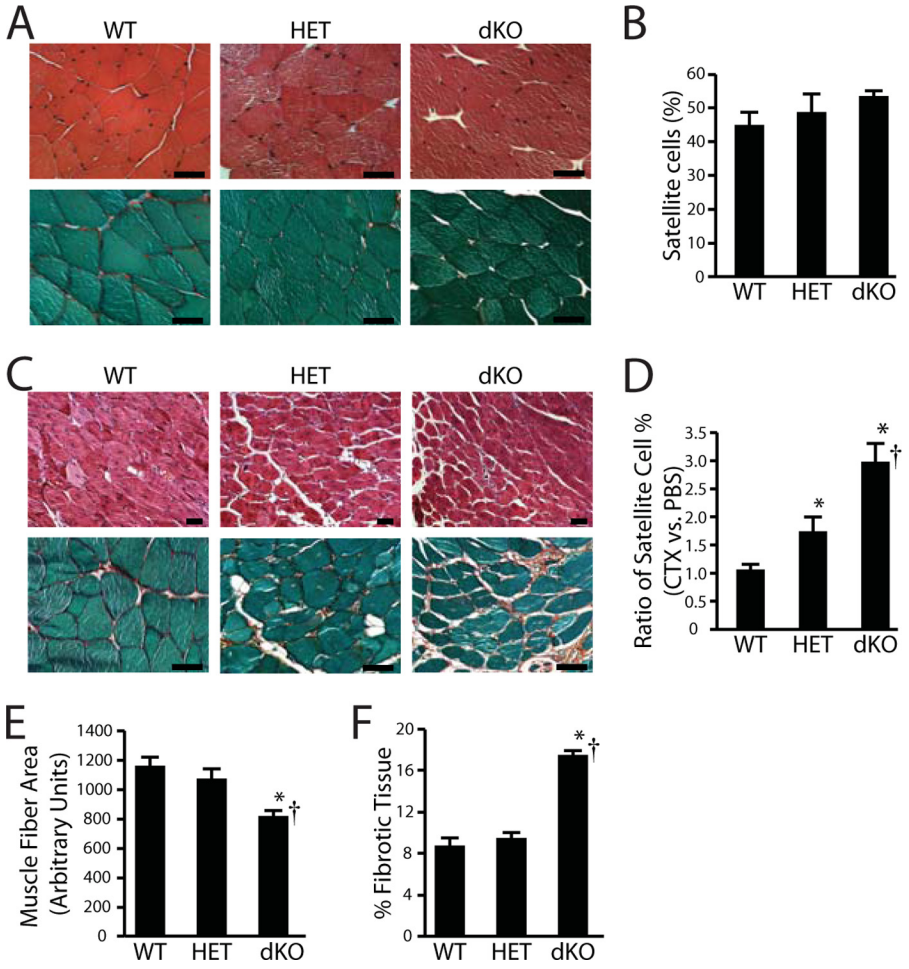

FIGURE 2. **CryAB is necessary for normal skeletal muscle regeneration.** *A*, CryAB WT, HET, and dKO mice 8–10 weeks of age are morphologically indistinguishable as determined by H&E (*upper*) and Sirius Red stains (*lower*). *B*, FACS analysis indicates the relative percentage of satellite cells in the mononuclear fraction isolated from 8–10-week CryAB WT, HET, and dKO muscle. *C–F*, mice were injected with CTX in the right TA muscle and sterile saline (vehicle control) in the left TA muscle. *C*, histological analysis by H&E stain (*upper*) and Sirius Red stain (*lower*) 2 weeks after CTX injury. *D*, ratio of satellite cells (CTX *versus* PBS vehicle) in CryAB WT, HET, and dKO muscle 14 days following CTX injections. *E*, quantification of muscle fiber size in CryAB WT, HET, and dKO muscle 14 days following CTX injections. *F*, quantification of fibrosis CryAB WT, HET, and dKO muscle 14 days following CTX injections. *Scale bars* are 50 μm. Statistical significance was set at $p < 0.05$ (*, with respect to WT, $n = 3$), and $p < 0.05$ (†, with respect to HET, $n = 3$).

cell and myoblast regulators contribute to the regeneration defects observed in CryAB dKO muscle.

To further understand why CryAB dKO mice experience age-dependent skeletal muscle atrophy, and why newly regenerated skeletal muscle is significantly smaller than in WT littermates after CTX injection, we looked at the expression of genes controlling hypertrophic growth and muscle atrophy. Under basal conditions, we observed a nearly 270% increase in the expression level of Atrogin-1 (*Fbxo32*) in dKO mice as compared with WT littermates (Fig. 3*E*). Atrogin-1 is a muscle-specific F-box E3-ubiquitin ligase known to be increased at the mRNA level prior to the onset of atrophy (35, 36). Although Atrogin-1 mRNA levels are reduced to ~40% of control in both WT and dKO mice following CTX treatment (Fig. 3*E*), the significant elevation of Atrogin-1 under basal conditions coupled with a significant reduction of *Mtor* to ~60% of control following CTX injury indicates that CryAB dKO mice are biased toward skeletal muscle atrophy.

CryAB Is a Novel Ago2-interacting Protein—The above observed uncoupling of protein expression and mRNA levels in CryAB dKO muscle undergoing regeneration prompted us to test the hypothesis that CryAB participates in the RNAi/miRNA pathway to regulate gene expression and muscle homeostasis. Previously, Iwasaki *et al.* (13) reported that *D. melanogaster* Hsc70 facilitated the loading of small RNA duplexes into Ago2. As such, we performed a Western blot screen for Ago2, CryAB, and Hsc70 in mouse tissues. Similar to previous studies, we observe high expression of CryAB in the heart and in skeletal muscle (Fig. 4*A*). Interestingly, these tissues also express the highest levels of Ago2, whereas Hsc70 is relatively ubiquitously expressed (Fig. 4*A*). We first performed co-immunoprecipitation assays of ectopically expressed Myc-Ago2 with FLAG-CryAB in HEK293T cells and found that CryAB interacts with Ago2 (Fig. 4*B*). We next tested whether CryAB interacts with other Argonaute proteins, as well as other proteins in the miRNA/RNAi functional pathway. In co-immunoprecipitation experiments with ectopic Myc-tagged Ago1, Ago2, Dicer, and DGCR8, FLAG-CryAB was found to specifically interact with Argonautes 1 and 2, but not with Dicer or DGCR8 (Fig. 4*B*). These results clearly demonstrate specificity of CryAB with respect to Argonaute proteins within the RNAi pathway.

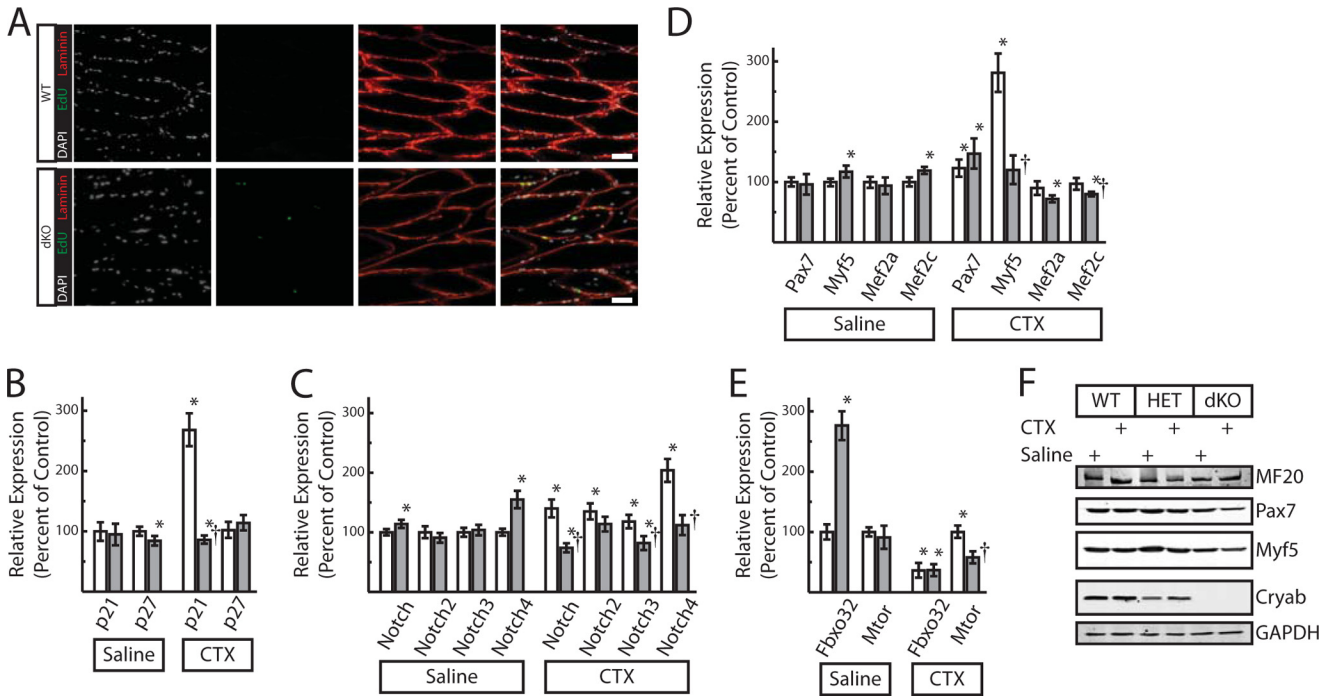

FIGURE 3. **CryAB is necessary for normal cellular proliferation and gene expression during skeletal muscle regeneration.** *A*, EdU incorporation in cells occupying the satellite cell niche 14 days after CTX injection. *Scale bar* is 50 μm. *B–E,* quantitative PCR analysis of changes in gene expression. Basal levels of gene expression were in left TA muscle (*Saline*) were quantified in both WT (*white bar*) and dKO (*gray bar*) littermates. Changes in gene expression following CTX injury were normalized to that of saline-injected control for both WT (*white bar*) and dKO (*gray bar*) littermates. Analyses were performed 14 days following CTX injections (*B–D*). Statistical significance was set at $p < 0.05$ (*, with respect to control, †, with respect to WT, $n = 6$, 3 male and 3 female). *F*, representative Western blots of lysates obtained from the right (CTX) and left (control) TA muscles.

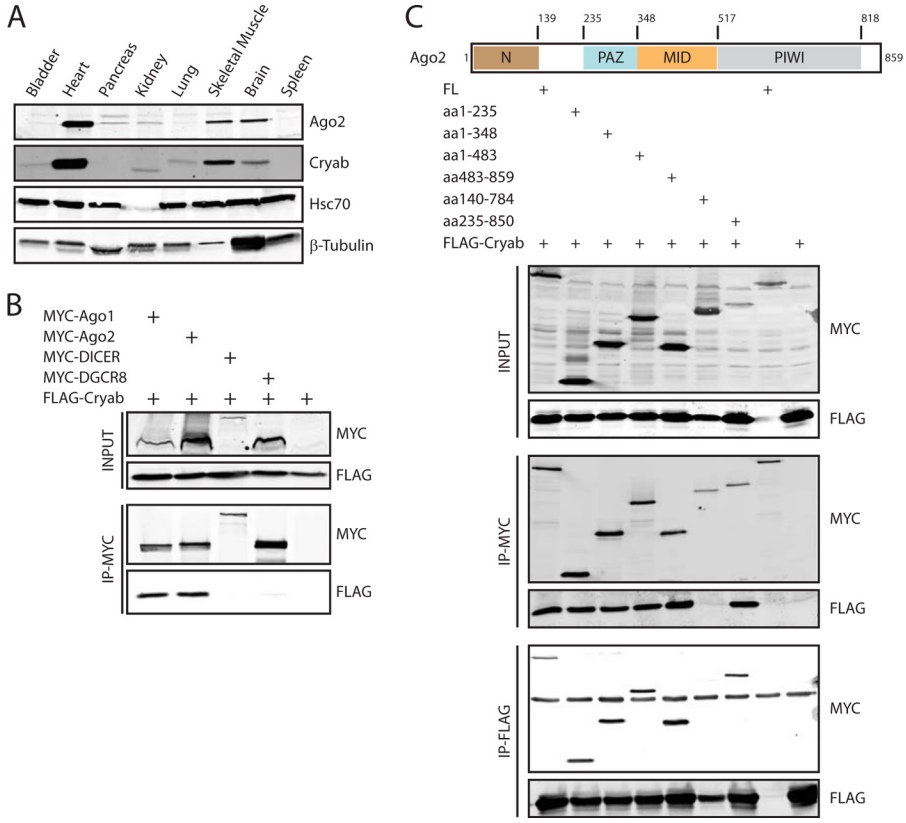

FIGURE 4. **CryAB interacts with Argonaute proteins.** *A*, Western blot analysis of the expression of Ago2, CryAB, Hsc70, and β-tubulin proteins in adult mouse tissues. Approximately 60 μg of total protein was loaded into each lane. *B*, co-immunoprecipitations of FLAG-CryAB with the indicated Myc-tagged proteins involved in miRNA biogenesis and RISC. *IP*, immunoprecipitation. *C*, co-immunoprecipitations of FLAG-CryAB with Myc-tagged truncations of full-length (*FL*) Ago2. *aa*, amino acids.

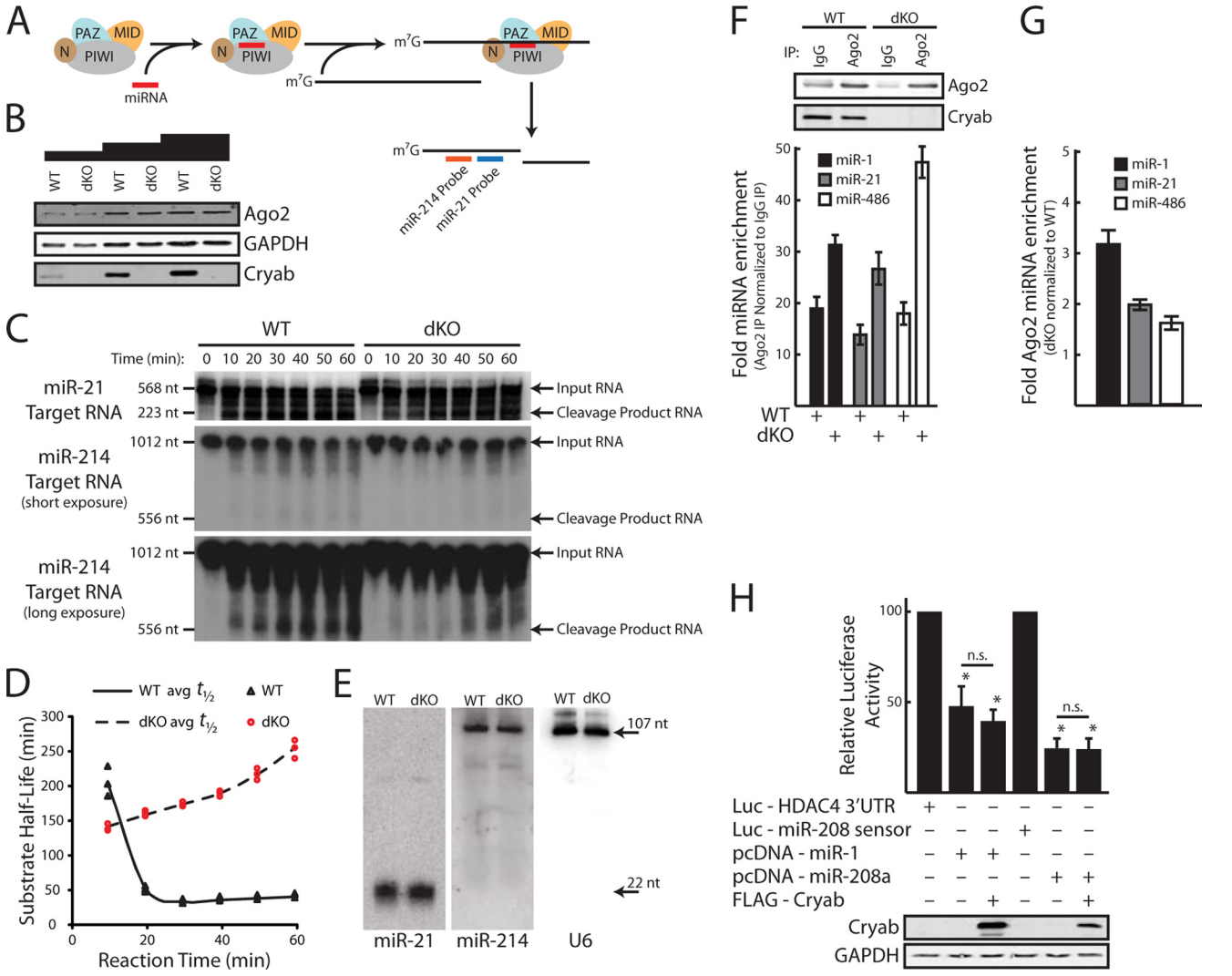

FIGURE 5. **Normal RISC activity is dependent upon CryAB expression.** *A*, schematic representation of the *in vitro* cleavage assay. *B*, Western blot of lysates from skeletal muscle of WT and CryAB dKO mice for use in miRNA-directed RNA cleavage assay. *C*, Northern analysis of miRNA-directed cleavage reactions at the indicated time points. MiRNA was preincubated with lysates for 20 min prior to the addition of 0.5 pmol of 5′-m^{7}G-capped RNA target. *nt*, nucleotides. *D*, effective miR-21 substrate half-life as a function of reaction time. *E*, Northern blot analysis of miRNA expression in hind limb skeletal muscle from WT and dKO littermates. *F*, Ago2 RNA immunoprecipitation (*IP*) assay from hind limb skeletal muscle of WT and dKO littermates. *Upper*, representative Western analysis of Ago2 and CryAB in the precipitates. *G*, -fold enrichment of Ago2 precipitated miRNAs between dKO and WT and normalized to precipitated Ago2 protein. *H*, luciferase (*Luc*) reporter assay utilizing the partially complementary HDAC4 3′-UTR and a perfectly complementary miR-208 sensor in the presence and absence of CryAB. Statistical significance was set at $p < 0.05$ (*, with respect to control, $n = 3$).

The recent crystal structure of human Ago2 by Schirle and MacRae (8) revealed a bilobed structure whose constituent four globular domains (N, PAZ, MID, and PIWI) individually align similarly to other prokaryotic and eukaryotic Argonautes, suggesting strong structural conservation of domain architecture. To identify the region of Ago2 necessary for the Ago2/CryAB interaction, we performed additional Ago2/CryAB co-immunoprecipitation experiments with Ago2 domain truncation mutants. N-terminal truncation mutants indicate that CryAB interacts with amino acids 1–235 of Ago2, whereas C-terminal truncation mutants indicate that CryAB interacts with amino acids 483–859 of Ago2 (Fig. 4*C*). Interestingly, CryAB does not interact with Ago2 amino acids 140–784, indicating that the N- and C-terminal regions of Ago2 are necessary for its interaction with CryAB. Amino acids 140–784 roughly correspond to the linker region after the globular N-terminal domain, the MID and PAZ domains, as well as the majority of the PIWI domain (Fig. 4*C*). Together, these results indicate that CryAB does not interact with the active catalytic site formed by the convergence of the MID, PAZ, and PIWI domains to enclose miRNA and the target strand RNA, but rather that CryAB may bind to a previously unidentified allosteric regulatory site of Ago2.

CryAB Positively Modulates Ago2 Endonuclease Activity—To determine whether the molecular function of CryAB with respect to Ago2 is that of an allosteric activator or inhibitor, we measured the time dependence of miRNA-directed RNA cleavage with muscle tissue lysates from CryAB dKO and WT control mice. Tissue lysates contain all the necessary biochemical machinery to load the miRNA and target RNA into RISC, as well as to cleave the target RNA in a miRNA sequence-specific manner (Fig. 5*A*). Western analysis of WT and CryAB dKO lysates confirms equal protein content of both Ago2 and GAPDH (Fig. 5*B*). In WT lysates preincubated with either miR-21 or miR-214, we detect cleavage product accumulation

as early as 10 min following the addition of m^7G-capped RNA substrate (Fig. 5*C*). Although we do observe cleavage product from dKO lysates, we do not observe depletion of the 568-nucleotide miR-21 target RNA by 60 min as we do with WT lysates. We next quantified miR-21-mediated cleavage product and remaining RNA substrate signal intensities at all measured time points. Calculation of the effective half-life ($t_{½}$) for the miR-21 substrate (Fig. 5*C*, *top*) as a function of reaction time further supports our hypothesis of CryAB being an allosteric activator of Ago2 (Fig. 5*D*). We calculate an average effective $t_{½}$ of 67 and 189 min with WT and Cryab dKO lysates, respectively. Further, 30 min after the addition of substrate, our miR-21 substrate RNA has an effective $t_{½}$ of 32 and 174 min with WT and CryAB dKO lysates, respectively. Similarly, detection of the cleavage product from the 1012-nucleotide miR-214 target RNA is detected as early as 10 min with WT lysates, but not until ~40–50 min with CryAB dKO lysates (Fig. 5*C*, *bottom*). Together, these data strongly suggest that the observed repression of miRNA-directed Ago2-dependent endonuclease activity in the absence of CryAB is independent of miRNA/substrate RNA.

To determine whether our observed difference in the *in vitro* mRNA $t_{½}$ is due to alterations in miRNA expression *in vivo* that may impact our assay, we measured miRNA expression by Northern blot (Fig. 5*E*). We observe no significant alterations in either the expression or the maturation of miR-21 and miR-214 in dKO muscle as compared with WT. Next, we sought to determine whether our observed difference in the *in vitro* mRNA $t_{½}$ is due to an alteration in the ability of RISC to load miRNA in the absence of CryAB. We then performed an Ago2 RNA immunoprecipitation and quantified the relative amount of miRNAs that co-immunoprecipitate with Ago2 *in vivo* (Fig. 5, *F* and *G*). We observe >20-fold enrichment of miRNAs 1, 21, and 486 in Ago2 immunoprecipitates as compared with IgG control (Fig. 5*F*). To control for the amount of Ago2 precipitated, we next normalized the relative amount of miRNA enriched in the Ago2 precipitates between WT and dKO to the amount of Ago2 in each precipitation reaction. Unexpectedly, we observe statistically significant enrichment of miRNAs 1, 21, and 486 in dKO as compared with WT (Fig. 5*G*). Together, these results indicate that in the absence of CryAB, Ago2/RISC is greatly enriched in miRNAs, likely contributing to its functional deficit. Finally, we performed luciferase assays to determine whether CryAB would affect miRNA complementary binding-mediated translational repression. We observe that exogenous CryAB does not enhance miRNA-mediated repression of luciferase activity of either the partial complementary HDAC4 3′-UTR or the perfectly complementary miR-208 sensor (Fig. 5*H*).

DISCUSSION

Our data indicate that miRNA-directed Ago2 endonuclease activity is positively regulated by CryAB in skeletal muscle. Given the necessity of Ago2 for normal mammalian development (6), it is unsurprising that a modest, but significant, change in Ago2/miRNA/RNA enzyme kinetics would result in a progressive chronic muscle phenotype observable with advanced age. In our acute regenerative model, we similarly observe reduced myofiber hypertrophic growth in CryAB dKO mice as compared with WT littermates. Our data indicate that in skeletal muscle, the absence of CryAB/Hspb2 results in the hypertrophy-atrophy axis being biased toward atrophy. Further, our observation that miR-21 is greatly enriched in Ago2/RISC of CryAB dKO mice would suggest that miR-21-mediated repression of cognate genes is enhanced. This is consistent with our observations of increased fibrosis and impaired hypertrophic growth in regenerating skeletal muscle, as inhibition of miR-21 has been previously demonstrated to significantly decrease fibrosis and hypertrophy in myocardial disease (37).

In addition to the other well documented functions of CryAB, our data strongly suggest that CryAB is necessary for normal miRNA-directed Ago2 endonuclease activity in skeletal muscle. In the *D. melanogaster* model system, prior studies have documented enhanced siRNA/miRNA-directed Ago2 endonuclease activity in the presence of RNA-binding proteins (11, 12). Despite its lack of an RNA binding domain and intrinsic ATPase activity (38), our data indicate that CryAB functions as a positive allosteric regulator of Ago2/RISC. Interestingly, CryAB appears to act by preventing excessive miRNA loading into Ago2/RISC, as the absence of CryAB resulted in greater enrichment of miRNAs.

Mechanistically it has been reported that: (i), highly complementary target RNAs accelerate the release of miRNAs from human Ago2 (39), (ii) *D. melanogaster* Ago2 directly receives the miRNA-miRNA* duplex and cleaves the miRNA* (passenger strand), facilitating its displacement and thus activation of RISC (40), and (iii) mRNA targets in *Caenorhabditis elegans* can protect cognate miRNAs from exonuclease-dependent degradation (41, 42). Our observations of an increased RNA $t_{½}$ with a perfectly complementary cognate miRNA and increased miRNA loading in Ago2 are consistent with CryAB playing a role in i) unloading of miRNA and/or target RNA, ii) miRNA-miRNA* duplex separation and RISC activation, and iii) protection of miRNAs from degradation. However, given that CryAB physically interacts only with the N and C termini, rather than the catalytic site of the Ago2 protein, this third possibility would likely be dependent upon steric hindrance of the Ago2 catalytic cleft by multimeric CryAB complexes. These intriguing hypotheses remain open for investigation. Together, our studies link the function of CryAB to the miRNA/RNAi pathway and suggest that aberrant modulation of miRNA-directed Ago2-dependent endonuclease activity may be implicated in the progression of disease.

Acknowledgments—We thank members of the Wang laboratory for advice and support. We thank Xiaoyun Hu for excellent technical assistance. We thank Dr. Eric Wawrousek for the Cryab/Hspb2 mouse line. We thank Drs. Robert Nakamoto and Jianming Liu for many helpful conversations, and we thank Dr. Jian Ding for help with the Argonaute2 RNA immunoprecipitation.

REFERENCES

1. Kim, V. N. (2005) MicroRNA biogenesis: coordinated cropping and dicing. *Nat. Rev. Mol. Cell Biol.* **6,** 376–385
2. Bartel, D. P. (2009) MicroRNAs: target recognition and regulatory functions. *Cell* **136,** 215–233

3. Djuranovic, S., Nahvi, A., and Green, R. (2011) A parsimonious model for gene regulation by miRNAs. *Science* **331,** 550–553
4. Bartel, D. P. (2004) MicroRNAs: genomics, biogenesis, mechanism, and function. *Cell* **116,** 281–297
5. Meister, G., Landthaler, M., Patkaniowska, A., Dorsett, Y., Teng, G., and Tuschl, T. (2004) Human Argonaute2 mediates RNA cleavage targeted by miRNAs and siRNAs. *Mol. Cell* **15,** 185–197
6. Liu, J., Carmell, M. A., Rivas, F. V., Marsden, C. G., Thomson, J. M., Song, J. J., Hammond, S. M., Joshua-Tor, L., and Hannon, G. J. (2004) Argonaute2 is the catalytic engine of mammalian RNAi. *Science* **305,** 1437–1441
7. Song, J. J., Smith, S. K., Hannon, G. J., and Joshua-Tor, L. (2004) Crystal structure of Argonaute and its implications for RISC slicer activity. *Science* **305,** 1434–1437
8. Schirle, N. T., and MacRae, I. J. (2012) The crystal structure of human Argonaute2. *Science* **336,** 1037–1040
9. Selbach, M., Schwanhäusser, B., Thierfelder, N., Fang, Z., Khanin, R., and Rajewsky, N. (2008) Widespread changes in protein synthesis induced by microRNAs. *Nature* **455,** 58–63
10. Ebert, M. S., and Sharp, P. A. (2012) Roles for microRNAs in conferring robustness to biological processes. *Cell* **149,** 515–524
11. Liu, Q., Rand, T. A., Kalidas, S., Du, F., Kim, H. E., Smith, D. P., and Wang, X. (2003) R2D2, a bridge between the initiation and effector steps of the *Drosophila* RNAi pathway. *Science* **301,** 1921–1925
12. Liu, Y., Ye, X., Jiang, F., Liang, C., Chen, D., Peng, J., Kinch, L. N., Grishin, N. V., and Liu, Q. (2009) C3PO, an endoribonuclease that promotes RNAi by facilitating RISC activation. *Science* **325,** 750–753
13. Iwasaki, S., Kobayashi, M., Yoda, M., Sakaguchi, Y., Katsuma, S., Suzuki, T., and Tomari, Y. (2010) Hsc70/Hsp90 chaperone machinery mediates ATP-dependent RISC loading of small RNA duplexes. *Mol. Cell* **39,** 292–299
14. Aquilina, J. A., Benesch, J. L., Bateman, O. A., Slingsby, C., and Robinson, C. V. (2003) Polydispersity of a mammalian chaperone: mass spectrometry reveals the population of oligomers in αB-crystallin. *Proc. Natl. Acad. Sci. U.S.A.* **100,** 10611–10616
15. Braun, N., Zacharias, M., Peschek, J., Kastenmüller, A., Zou, J., Hanzlik, M., Haslbeck, M., Rappsilber, J., Buchner, J., and Weinkauf, S. (2011) Multiple molecular architectures of the eye lens chaperone αB-crystallin elucidated by a triple hybrid approach. *Proc. Natl. Acad. Sci. U.S.A.* **108,** 20491–20496
16. Fink, A. L. (1999) Chaperone-mediated protein folding. *Physiol. Rev.* **79,** 425–449
17. Ousman, S. S., Tomooka, B. H., van Noort, J. M., Wawrousek, E. F., O'Connor, K. C., Hafler, D. A., Sobel, R. A., Robinson, W. H., and Steinman, L. (2007) Protective and therapeutic role for αB-crystallin in autoimmune demyelination. *Nature* **448,** 474–479
18. van Noort, J. M., van Sechel, A. C., Bajramovic, J. J., el Ouagmiri, M., Polman, C. H., Lassmann, H., and Ravid, R. (1995) The small heat-shock protein αB-crystallin as candidate autoantigen in multiple sclerosis. *Nature* **375,** 798–801
19. Iwaki, T., Kume-Iwaki, A., Liem, R. K., and Goldman, J. E. (1989) αB-crystallin is expressed in non-lenticular tissues and accumulates in Alexander's disease brain. *Cell* **57,** 71–78
20. Fuchs, E., and Cleveland, D. W. (1998) A structural scaffolding of intermediate filaments in health and disease. *Science* **279,** 514–519
21. Vicart, P., Caron, A., Guicheney, P., Li, Z., Prévost, M. C., Faure, A., Chateau, D., Chapon, F., Tomé, F., Dupret, J. M., Paulin, D., and Fardeau, M. (1998) A missense mutation in the αB-crystallin chaperone gene causes a desmin-related myopathy. *Nat. Genet.* **20,** 92–95
22. Wang, X., Osinska, H., Klevitsky, R., Gerdes, A. M., Nieman, M., Lorenz, J., Hewett, T., and Robbins, J. (2001) Expression of R120G-αB-crystallin causes aberrant desmin and αB-crystallin aggregation and cardiomyopathy in mice. *Circ. Res.* **89,** 84–91
23. Rajasekaran, N. S., Connell, P., Christians, E. S., Yan, L. J., Taylor, R. P., Orosz, A., Zhang, X. Q., Stevenson, T. J., Peshock, R. M., Leopold, J. A., Barry, W. H., Loscalzo, J., Odelberg, S. J., and Benjamin, I. J. (2007) Human αB-crystallin mutation causes oxido-reductive stress and protein aggregation cardiomyopathy in mice. *Cell* **130,** 427–439
24. Brady, J. P., Garland, D. L., Green, D. E., Tamm, E. R., Giblin, F. J., and Wawrousek, E. F. (2001) αB-crystallin in lens development and muscle integrity: a gene knockout approach. *Invest. Ophthalmol. Vis. Sci.* **42,** 2924–2934
25. Cheung, T. H., Quach, N. L., Charville, G. W., Liu, L., Park, L., Edalati, A., Yoo, B., Hoang, P., and Rando, T. A. (2012) Maintenance of muscle stem-cell quiescence by microRNA-489. *Nature* **482,** 524–528
26. Stabile, E., Burnett, M. S., Watkins, C., Kinnaird, T., Bachis, A., la Sala, A., Miller, J. M., Shou, M., Epstein, S. E., and Fuchs, S. (2003) Impaired arteriogenic response to acute hindlimb ischemia in CD4-knockout mice. *Circulation* **108,** 205–210
27. Stabile, E., Kinnaird, T., la Sala, A., Hanson, S. K., Watkins, C., Campia, U., Shou, M., Zbinden, S., Fuchs, S., Kornfeld, H., Epstein, S. E., and Burnett, M. S. (2006) $CD8^+$ T lymphocytes regulate the arteriogenic response to ischemia by infiltrating the site of collateral vessel development and recruiting $CD4^+$ mononuclear cells through the expression of interleukin-16. *Circulation* **113,** 118–124
28. Huang, Z. P., Chen, J. F., Regan, J. N., Maguire, C. T., Tang, R. H., Dong, X. R., Majesky, M. W., and Wang, D. Z. (2010) Loss of microRNAs in neural crest leads to cardiovascular syndromes resembling human congenital heart defects. *Arterioscler. Thromb. Vasc. Biol.* **30,** 2575–2586
29. Huang, Z. P., Neppl, R. L., Jr., and Wang, D. Z. (2011) Application of microRNA in cardiac and skeletal muscle disease gene therapy. *Methods Mol. Biol.* **709,** 197–210
30. Chen, J. F., Mandel, E. M., Thomson, J. M., Wu, Q., Callis, T. E., Hammond, S. M., Conlon, F. L., and Wang, D. Z. (2006) The role of microRNA-1 and microRNA-133 in skeletal muscle proliferation and differentiation. *Nat. Genet.* **38,** 228–233
31. Callis, T. E., Pandya, K., Seok, H. Y., Tang, R. H., Tatsuguchi, M., Huang, Z. P., Chen, J. F., Deng, Z., Gunn, B., Shumate, J., Willis, M. S., Selzman, C. H., and Wang, D. Z. (2009) MicroRNA-208a is a regulator of cardiac hypertrophy and conduction in mice. *J. Clin. Invest.* **119,** 2772–2786
32. Chakkalakal, J. V., Jones, K. M., Basson, M. A., and Brack, A. S. (2012) The aged niche disrupts muscle stem cell quiescence. *Nature* **490,** 355–360
33. Carlson, M. E., Hsu, M., and Conboy, I. M. (2008) Imbalance between pSmad3 and Notch induces CDK inhibitors in old muscle stem cells. *Nature* **454,** 528–532
34. Conboy, I. M., Conboy, M. J., Smythe, G. M., and Rando, T. A. (2003) Notch-mediated restoration of regenerative potential to aged muscle. *Science* **302,** 1575–1577
35. Gomes, M. D., Lecker, S. H., Jagoe, R. T., Navon, A., and Goldberg, A. L. (2001) Atrogin-1, a muscle-specific F-box protein highly expressed during muscle atrophy. *Proc. Natl. Acad. Sci. U.S.A.* **98,** 14440–14445
36. Sandri, M., Sandri, C., Gilbert, A., Skurk, C., Calabria, E., Picard, A., Walsh, K., Schiaffino, S., Lecker, S. H., and Goldberg, A. L. (2004) Foxo transcription factors induce the atrophy-related ubiquitin ligase atrogin-1 and cause skeletal muscle atrophy. *Cell* **117,** 399–412
37. Thum, T., Gross, C., Fiedler, J., Fischer, T., Kissler, S., Bussen, M., Galuppo, P., Just, S., Rottbauer, W., Frantz, S., Castoldi, M., Soutschek, J., Koteliansky, V., Rosenwald, A., Basson, M. A., Licht, J. D., Pena, J. T., Rouhanifard, S. H., Muckenthaler, M. U., Tuschl, T., Martin, G. R., Bauersachs, J., and Engelhardt, S. (2008) MicroRNA-21 contributes to myocardial disease by stimulating MAP kinase signalling in fibroblasts. *Nature* **456,** 980–984
38. Horwitz, J. (2003) α-crystallin. *Exp. Eye Res.* **76,** 145–153
39. De, N., Young, L., Lau, P. W., Meisner, N. C., Morrissey, D. V., and MacRae, I. J. (2013) Highly complementary target RNAs promote release of guide RNAs from human Argonaute2. *Mol. Cell* **50,** 344–355
40. Matranga, C., Tomari, Y., Shin, C., Bartel, D. P., and Zamore, P. D. (2005) Passenger-strand cleavage facilitates assembly of siRNA into Ago2-containing RNAi enzyme complexes. *Cell* **123,** 607–620
41. Chatterjee, S., Fasler, M., Büssing, I., and Grosshans, H. (2011) Target-mediated protection of endogenous MicroRNAs in *C. elegans*. *Dev. Cell* **20,** 388–396
42. Chatterjee, S., and Grosshans, H. (2009) Active turnover modulates mature microRNA activity in *Caenorhabditis elegans*. *Nature* **461,** 546–549